

Bézier-based metamaterials: Synthesis, mechanics and additive manufacturing

Alberto Álvarez-Trejo^{a,1}, Enrique Cuan-Urquiza^{a,1,*}, Armando Roman-Flores^b, L.G. Trapaga-Martinez^c, J.M. Alvarado-Orozco^d

^a Tecnológico de Monterrey, School of Engineering and Sciences, Epigmenio González 500 Fracc, San Pablo, Querétaro 76130, Mexico

^b Tecnológico de Monterrey, School of Engineering and Sciences, General Ramon Corona 2514, Zapopan 45138, Mexico

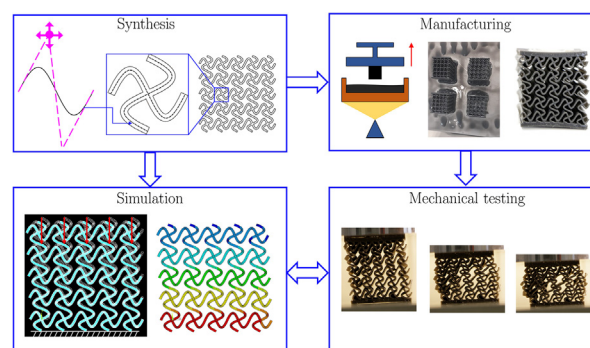
^c CIATEQ Centro de Tecnología Avanzada, Querétaro 76150, Santiago de Querétaro, Mexico

^d Center of Engineering and Industrial Development, CIDEI, Surface Engineering and Additive Manufacturing Department, Querétaro, Av. Pie de la Cuesta 702, 76125, Santiago de Querétaro, Mexico

HIGHLIGHTS

- A novel method for the synthesis of spiral-based cubic Bézier metamaterials is presented.
- Apparent stiffness was characterized via additively manufactured samples and computational simulations.
- Apparent Young's modulus is related to the mathematical parametrization of the curves conforming the structures.
- The synthesis method allows the control of the form of the stress-strain curves of the metamaterials.
- Apparent stiffness decreases proportionally to the cubic root of the distance from the control point to the unit cell center.

GRAPHICAL ABSTRACT



ARTICLE INFO

Article history:

Received 27 November 2020

Received in revised form 10 December 2020

Accepted 13 December 2020

Available online 17 December 2020

Keywords:

Metamaterials

Apparent mechanical properties

Structure-property relationship

Cubic Bézier curves

Lattice

Additive manufacturing

ABSTRACT

The design of mechanical metamaterials often uses lattice arrangements being benefited from the increase in Additive Manufacturing technologies available. Such design freedom allows the fabrication of lattice arrangements with complex curved geometries. Here we propose a whole family of novel lattice metamaterials parametrized using cubic Bézier curves. The methodology presented permits the generation of unit cells with different degrees of curvature based on the location of the Bézier control points along a spiral. The apparent stiffness of these structures was characterized using finite element analysis and compression tests on additively manufactured samples using stereolithography. The mechanical properties of spiral based cubic Bézier metamaterials were related to the location of the control points, curvature, etc. It was found that the apparent stiffness decreases proportionally to the cubic root of the distance between the control point and the predefined origin of the coordinate system. Due to symmetry conditions, the slope continuity in the curves conforming the unit cells is fulfilled and the origin of the coordinate system used coincides with the center of the unit cells. The procedure presented for the synthesis of metamaterials enables the generation of structures with customized mechanical properties by adjusting the geometry of the unit cells.

© 2020 The Authors. Published by Elsevier Ltd. This is an open access article under the CC BY-NC-ND license (<http://creativecommons.org/licenses/by-nc-nd/4.0/>).

* Corresponding author.

E-mail address: ecuanurqui@tec.mx (E. Cuan-Urquiza).

¹ These authors are part of the Metamaterials Lab group at Tecnológico de Monterrey, Campus Querétaro.

1. Introduction

Progress in fabrication technologies, such as additive manufacturing (AM), has increased design freedom for engineering applications. One approach to optimizing parts consists on using lattices or cellular materials, more recently known as *metamaterials*. Metamaterials possess various advantages over fully dense structures, but further study on their mechanical behaviour is needed to better suit engineering requirements.

Optimized use of materials within a structure can be found in different examples in nature, e.g., trabecular bone, honeycombs, wood, and sponges [1,2]. These have inspired the design and engineering communities. Designing with metamaterials has several advantages, which are found in nature: minimal use of material, high strength to weight ratio [2], energy absorption, and high compliance [3]. Potential applications for metamaterials include vibration and heat insulators [4], as well as sandwich panels, due to their light weight. Another potential use for metamaterials is in implantable mechanical devices (e.g., knee and hip implants, and stents) [5,6].

Mechanical metamaterials are normally described by their *apparent properties*. These properties are those that, when the dimensions of the elements conforming the lattice are significantly smaller than the macro dimensions of the structure they are *filling*, represent the properties as if the metamaterial is homogeneous with equivalent continuum properties.

1.1. Synthesis of curve-based metamaterials

Lattice metamaterials make use of beams, struts, and rods to form their structure. While these lattice elements are commonly found to be straight, *curved* elements have been also used in metamaterial design [7]: arcs [8–10], sine functions [11–13], and other complex curves [14,15].

Research has been carried out on the mechanical characterization of curve-based metamaterials, following different approaches, including analytical, computational, and experimental. Mechanical properties of metamaterials vary depending on the geometrical parameters that define the form of their elements [8]. The most frequent choice of curves when designing a curved-metamaterial is arcs, often combined with straight segments. An example is chiral structures [16–19]. In general, the deformation mechanisms of such metamaterials involve bending of the struts and rotation of the nodes (allowed by the presence of curved elements). Sinusoidal elements have also been used in metamaterial synthesis, improving crashworthiness [11] and a longer plateau region in the strain-stress curve [9,10] than their counterparts based on straight struts.

Other parametric curves that have been used in metamaterial design are those proposed by Wang et al. [14,15] who studied the deformation mechanism of a petal-shaped auxetic metamaterial based on non-uniform rational basis splines (NURBS) [14,15]. This base configuration is optimized, by means of isogeometric analysis (IGA), to obtain a desired Poisson's ratio by changing the control points position. Perturbation of mathematically parametrized curved-metamaterials was studied by Choi et al. [20]. In [20] authors analyzed unit cells based on B-splines computationally, altering the control point position to reach a desired negative Poisson's ratio. Despite that Bézier curves are frequently used in different computational and manufacturing applications [21–23], the use of them for the synthesis of metamaterials in conforming unit cells has not been studied, and even less the characterization of their apparent stiffness as a function of their mathematical parametrization. In comparison to other parametric curves, Bézier curves have fewer parameters, making the tuning of the curve simpler while keeping the complexity in shape.

1.2. Manufacturing of metamaterials

Stereolithography (SLA) is a vat-photopolymerization additive manufacturing technique that allows the fabrication of 3D objects with a high building speed and good part resolution [2]. This process

requires a vat filled with thermoset liquid resin that solidifies when exposed to electromagnetic radiation [24]. This radiation, usually an ultra-violet (UV) laser, traces and selectively cures the material, forming the desired model layer-by-layer. Once a layer is completed, the platform moves, coating the part with a new layer of resin [25].

Parts fabricated via SLA are anisotropic, as their mechanical properties depend on the building orientation; stiffness is higher if it is perpendicular to the loading direction [26]. They are also influenced by the curing process [27]; since the resin is solidified layer-by-layer, curing is not uniform, and the part can fail at the interface between layers. Furthermore, the resin does not fully polymerize during the SLA process [28]. Therefore, SLA printed parts can also be post-cured, usually with UV light of the same wavelength employed by the SLA printer. Differences are encountered between the mechanical properties of green (i.e., uncured) and UV-cured components [28].

SLA has been used in the fabrication of architected metamaterials previously. Alomarah et al. [17] fabricated a re-entrant chiral auxetic honeycomb using the VisiJet SL Flex polymer. Lin et al. [29] fabricated 3D trusses and gyroids, reinforcing the resin with graphene oxides and comparing the resulting mechanical properties in compression. Patel et al. [30] tested highly deformable 3D structures in compression. Keshavarzan et al. [31] studied the effect of porosity on the apparent mechanical properties of two different topologies of SLA-fabricated gyroids. As SLA has demonstrated to be a promising fabrication technology for producing lattice and porous metamaterials, we employ it here to fabricate the samples used to demonstrate the synthesis method presented.

The method for the synthesis of metamaterials based on cubic Bézier curves allows the generation of different unit cell designs by varying a single parameter that defines its curvature. This is described in Section 2. Section 3 includes the fabrication of selected metamaterial samples using SLA, their mechanical characterization with laboratory experiments, and computationally via Finite Element Analysis (FEA). The results of these procedures are presented in Section 4. Discussion on the deformation mechanism of the mechanical metamaterials designed here is elaborated in Section 5. Finally, some concluding remarks and insight into future work can be found in Section 6.

2. Synthesis of metamaterials with Bézier curves

The need for complex shapes in various design applications leads to the development of curves defined with parametric equations. Parametric equations allow a simple computational implementation along with better fitting to complex shapes [21]. Parametric equations are also the standard for complex curves in CAD systems, allowing rapid changes in geometry when altering their defining parameters. One of such parametric representations is *Bézier curves*, which are defined based on the *Bernstein function* [32]. The parametric equation for a Bézier curve is given as

$$B(t) = \sum_{i=0}^n \binom{n}{i} \mathbf{P}_i (1-t)^{n-i} t^i, \quad (1)$$

$$t \in [0, 1]$$

where \mathbf{P}_i represents the coordinate of every control point, as a complex number; n is the number of control points, which is one higher than the degree of the Bézier curve. This parametric representation is known as *de Casteljau's algorithm*. It allows to define the Bézier curve with a set of control points: an initial point P_0 , a final point P_n , and a set of intermediate points, that do not touch the curve, but define its shape. A cubic Bézier curve, containing 4 control points, is shown in Fig. 1a. The cubic Bézier is used in this work because changing only one of the four control points modifies the shape of the curve, given the restrictions to be presented; the unit cell can be defined in terms of its width and a single parameter defining shape.

2.1. Unit cell synthesis

The spiral-based cubic Bézier (SBCB) metamaterials proposed here are built from a minimal unit periodic repetition, known as *unit cell*. The method for the parametric design of 2D metamaterials based on cubic Bézier curves is described as follows. The unit cell consists of two cubic Bézier segments: B_1 which is horizontal and is presented in green colour in Fig. 1b, and B_2 which is vertical and is presented in blue in Fig. 1b. Segment B_1 is uniquely defined by a single control point (labelled as P_1 in Fig. 1b). This point is restricted to lie within a spiral centered at the origin, which is coincident with the midpoint of the curve. Segment B_2 is obtained by rotating segment B_1 by 90 degrees. An example of the metamaterial formed by periodically repeating a cubic Bézier-based unit cell is shown in Fig. 2.

For the pattern generation to be successful, slope continuity must be ensured in two adjacent unit cells. Therefore, linear segment $\overline{P_2P_3}$ in the first unit cell must be collinear with segment $\overline{P_0P_1}$ in an adjacent unit cell. This can be achieved if the control point P_2 is a double mirror of P_1 , as shown in Fig. 1b.

The presented definition of a unit cell allows the generation of different lattice metamaterials by changing the location of the control point P_1 . In order to generate a wide range of lattice patterns, the control point P_1 is placed on a spiral, granting the placement of the control point at different locations controlled by a single parametric curve. We define θ as the angle between the control polygon segment $\overline{P_1P_2}$ and the x -axis. Therefore, the angle θ becomes the only parameter defining the position of the control point P_1 . If the point P_1 is restricted to lie on a spiral centered at the origin, different distances from the origin to the location of P_1 can be generated with the variation of the angle θ .

In this way, the position of P_1 is defined only by the angle θ . To prove the concept presented here, point P_1 will be restricted within the interval $[0, 6\pi]$, or three complete turns of the spiral. Some additional parameters for the design of the SBCB unit cell are the following:

- The width of the unit cell is defined as λ . Given this, the starting point P_0 is fixed at $(-\lambda/2, 0)$ and the ending point P_3 is fixed at $(\lambda/2, 0)$. This choice makes the origin of the xy plane to be the midpoint of the base curve.
- The distance between the first control point P_1 and the origin is labelled as r . Considering the case of the spiral, this distance is defined as $r = \lambda\theta/4\pi$.

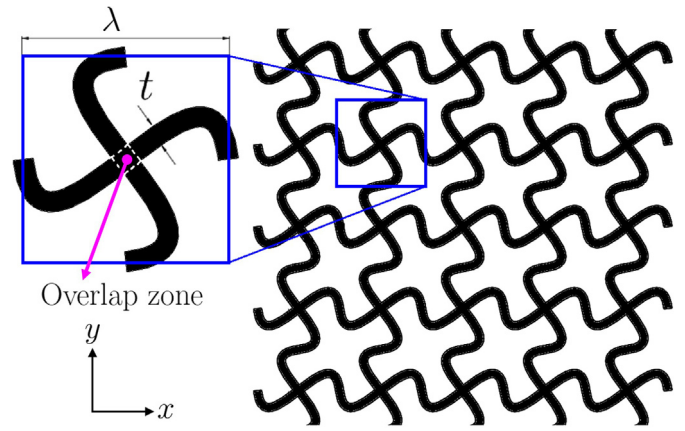


Fig. 2. Left: view of a unit cell. Right: view of the corresponding 5×5 lattice pattern. Key parameters of the unit cell: width of the unit cell λ and thickness t are shown. The Bézier segments overlap at an area shown with dashed white lines.

- The first control point P_1 is (x_1, y_1) . The second control point P_2 , is located symmetrically with respect to P_1 from both the x - and y -axes, leading it to be $(-x_1, -y_1)$.

A wide range of the 5×5 arrangements that can be generated with this synthesis method is shown in supplementary file V1.

2.2. Relative density calculation

The relative density is calculated as the ratio between the in-plane area occupied by solid material and the unit cell's total external area. As the depth in the out-of-plane direction is constant, it is not considered. The unit cell area is λ^2 and the thickness of the Bézier-curved elements (see Fig. 2) is t . To find the area occupied by material, it must be multiplied by the length of the Bézier segment, which will be denoted as l . Note from Fig. 2 that the two Bézier segments overlap at a square of area t^2 , so this area must be subtracted from the area occupied by

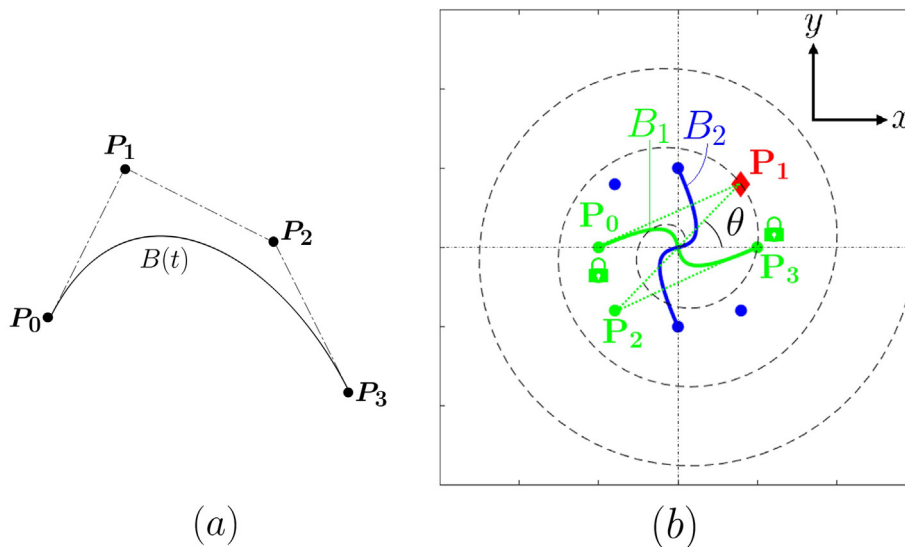


Fig. 1. (a) Cubic Bézier curve $B(t)$ and its corresponding control polygon, defined by the points P_0, P_1, P_2, P_3 . (b) Definition of a unit cell. We start by the original Bézier curve B_1 (in green) with its corresponding control polygon (dashed green lines). Points P_0 and P_3 are fixed. The independent control point P_1 (marked in red) always lies within the spiral, which is defined by the angle θ . The point P_2 is symmetric to point P_1 with respect to both axes. The second segment, B_2 , is shown in blue. Both segments conform a unit cell.

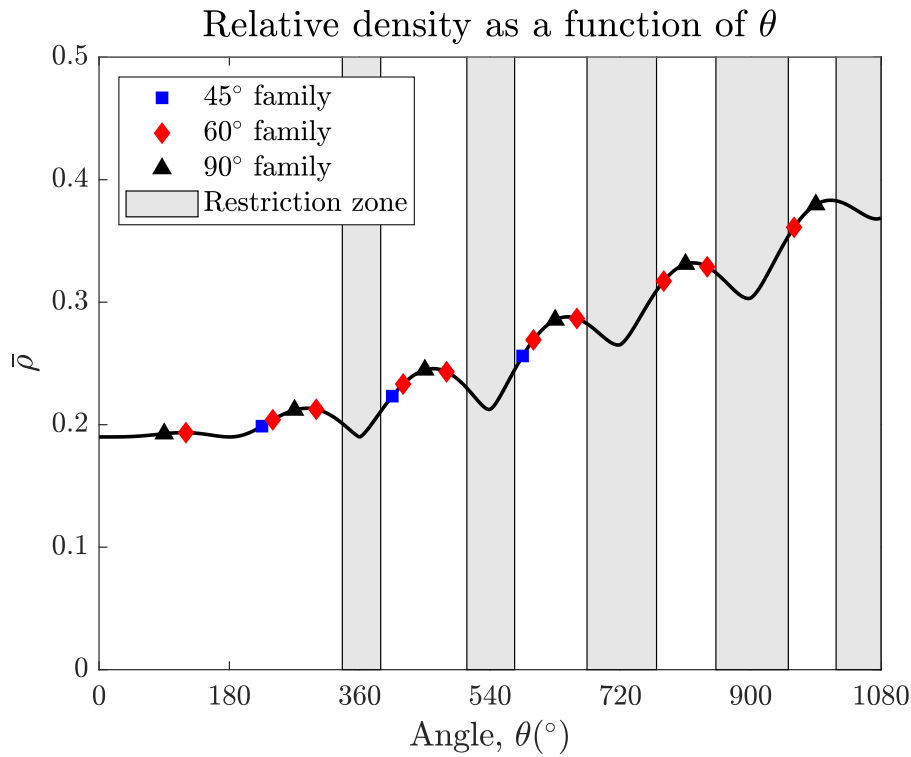


Fig. 3. Given $\lambda = 10$ and $t = 1$; plot showing how the relative density varies as the control points move along the spiral, hence moving further away from the origin. Markers indicate the designs studied here, separated by families.

material, which is twice the area of a single curved element. This results in the equation

$$\bar{\rho} = \frac{2lt - t^2}{\lambda^2} \tag{2}$$

The curve length is estimated from its discrete equivalent by summing the distances between contiguous points. From the unit cell definition, we have $\lambda = 10$ mm and $t = 1$ mm.

The relative density as a function of the angle θ is presented in Fig. 3. Note that the obtained relative densities increase, in general, with the angle θ , given that the only changing parameter is the length l of the Bézier curved element. Markers in Fig. 3 are the corresponding values of relative densities of the selected unit cells designs for fabrication in this study. Relative density values decrease near the multiples of 360° because curvature decreases, reducing the value of l as the unit cell becomes straighter.

2.3. Defining the concept of families of SBCB metamaterials

The selected designs of SBCB unit cells for this study are depicted in Fig. 4. Markers along the dashed line indicate the location of the control point P_1 in the plane. Here we group the generated structures into *families*, represented by different markers. Each family includes those structures that were formed by the angle θ and those formed by their complementing angles, regardless of the distance r from the origin. The complementing angles are θ , $-\theta$, $180^\circ - \theta$, and $180^\circ + \theta$ (see Fig. 5). These angles appear several times depending on the number of turns of the spiral (see Fig. 4). Now, consider the curves shown in Fig. 5, when these are used to conform unit cells and therefore lattice arrangements, all of these are mechanically equivalent when they are loaded in compression. This is due to identical curvature in each of the segments, given that the tangent lines in the control polygons have the same length and orientation. Fig. 5 also shows the equality in the

shape of every half of the cubic Bézier segment, given that the definition of the unit cell requires control points to be mirrored in both axes.

All the unit cells in Fig. 5 belong to the same family, as they were generated with complementing angles θ . In this work, we produced different unit cells by varying the angles and their complements grouped into three different families for the following angles: 45° , 60° , and 90° . Forcing the control points' location to lie on the spiral, when varying the angle θ , we obtained different unit cells as the distance from the origin r is changing. The three different families used in this work and the θ angles used to conform the corresponding structures are listed in Table 1.

3. Materials and methods

3.1. Unit cell geometry definition

A set of CAD models was generated for both FEA simulations and SLA additive manufacturing. For a rapid CAD file generation, a MATLAB® R2019a (Mathworks, Natick, United States) script was developed. Such script takes as input the desired set of angles θ , and a set of SOLIDWORKS® 2019 (Dassault Systèmes, Vélizy, France) macro files is obtained as output. These macro files contain the instructions to build a full CAD model of the lattice structures for the corresponding input parameters. Each lattice CAD model corresponds to a 5×5 unit cell repetition.

The control points obtained in Section 2 are used to sketch the cubic Bézier curves in SOLIDWORKS®. The curves are offset 0.5 mm in both directions, for a total thickness $t = 1$ mm, as shown in Fig. 6a. This thickness is suited for the manufacturing of the samples: a smaller value would complicate support generation and a larger value would lead to loss of the geometrical features. The unit cells are repeated 5 times in both the x - and y - directions, as shown in Fig. 6b. These 2D profiles are then extruded 50 mm in the z -axis. Solid plates with a thickness of 3 mm are also created at the upper and lower ends of the sample to

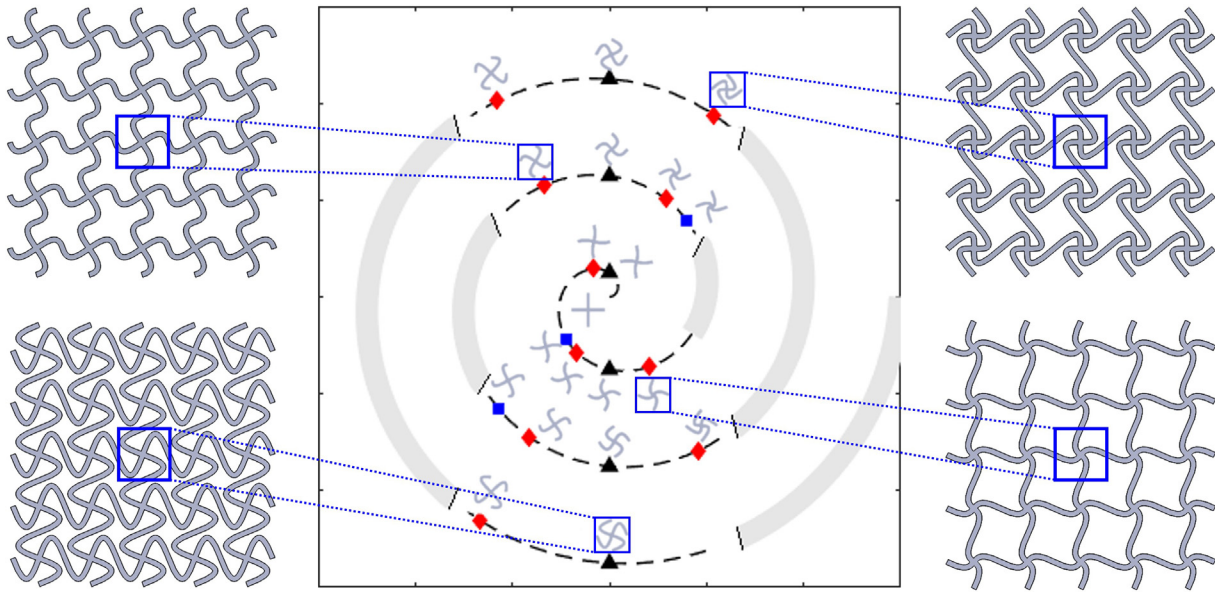


Fig. 4. Full spiral, showing the position of the control point P_1 for each design and its corresponding unit cell. As an example, 5×5 lattice arrangements formed by some of the unit cells are shown. Placing P_1 along the zones in gray does not produce valid geometries: see Appendix.

ensure a uniform loading distribution for further compression testing. An example of a complete CAD model is shown in Fig. 6c. Using this procedure, a total of 32 different CAD samples were generated.

It is impossible to offset a curve to a thickness greater than its minimum radius of curvature R because any curvature or continuity would be lost. Therefore, this feature must be considered for the unit cell synthesis. A detailed analysis of the curvature of the proposed structures can be found in the Appendix. The minimum radius of curvature for each base curve must be greater than the defined offset, 0.5 mm, for it to be feasible.

3.2. Finite element models setup

Finite element models for the 5×5 structures were developed using® ANSYS Mechanical APDL v20.1 (ANSYS Inc., Canonsburg, United States). These were meshed using SHELL181 [33], a four-node element defined by an area and a constant thickness. This type of element has been previously used to simulate similar lattice metamaterials [9,11,17]. The model was fed with the mechanical properties of the Formlabs® Flexible resin with Young's modulus of 5.08 MPa (obtained from tensile testing of dogbone SLA-samples, defined in Section 3.3)

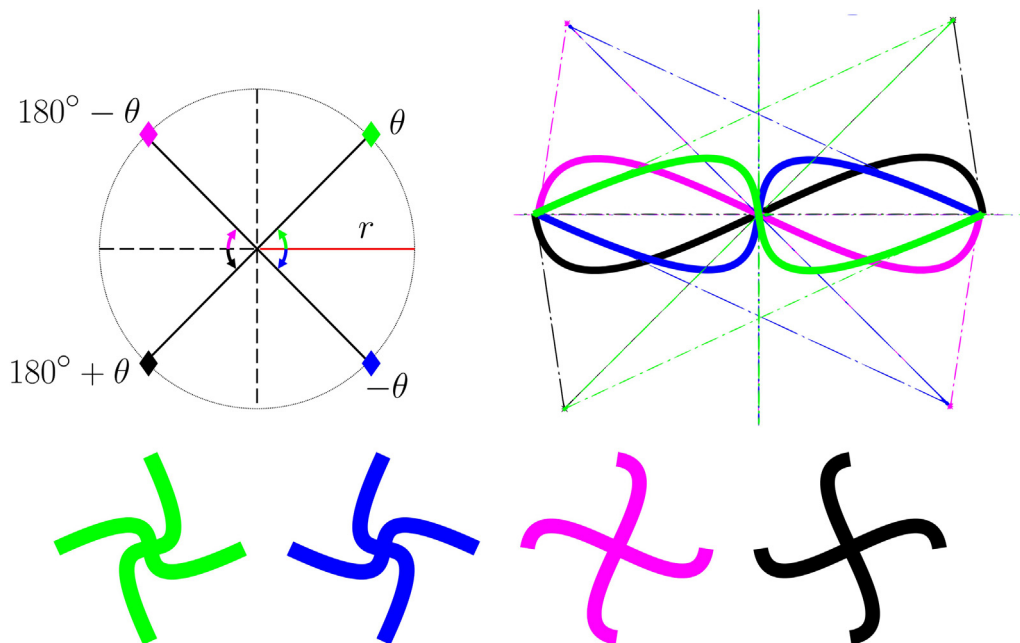


Fig. 5. Left: A circle with radius r , the markers are placed at the coordinates corresponding to the angles of a family: θ , $-\theta$, $180^\circ - \theta$, $180^\circ + \theta$. These are the possible positions for the control point P_1 for a given θ and r . Right: the cubic Bézier curves corresponding to each of the four P_1 points, along with their corresponding control polygons. Bottom: the resulting unit cells from the four equivalent curves. Colour scheme is kept the same for relating the corresponding unit cells to their forming curves.

Table 1

Base angles $\theta < 360^\circ$ for the generation of SBCB unit cells within a family. This set can be expanded by adding multiples of 360° to every possible angle, but the angles that were actually used are those depicted in Fig. 4.

Family	Base angles
45°	45°, 225°
60°	60°, 120°, 240°, 300°
90°	90°, 270°

and an assumed Poisson's ratio of 0.33. This is not reported by Formlabs® however, different values were simulated showing negligible differences in the response [34].

All the samples were meshed with a single shell element throughout the thickness (z-axis in Fig. 6). Each curved segment was meshed with 50 rectangular elements to approximate the curvature. In order to match the geometry of the actual manufactured samples, the shell thickness was set to be 1 mm.

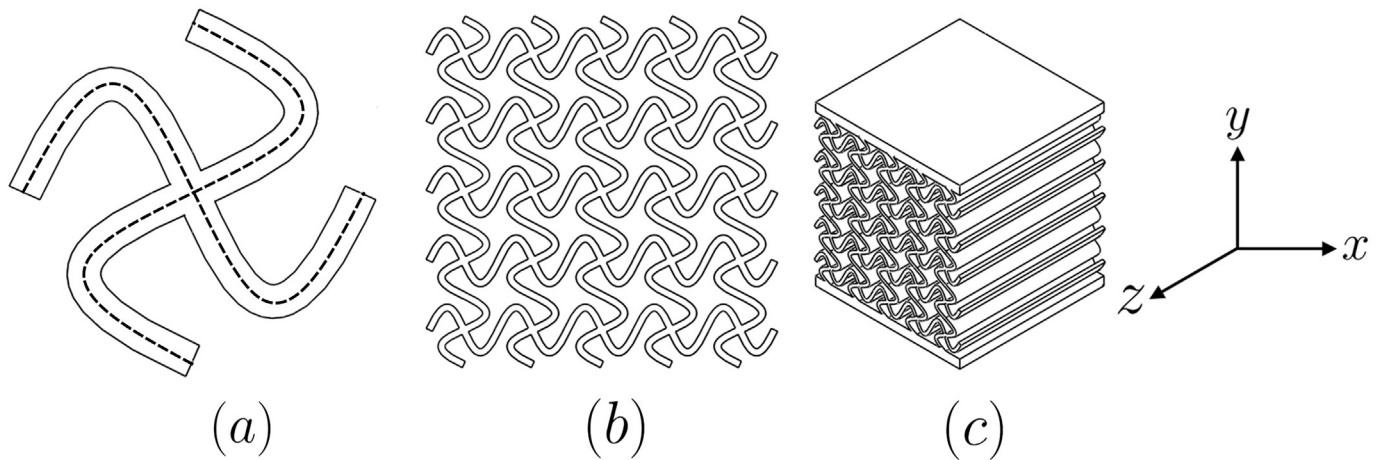


Fig. 6. (a) Unit cell, showing the cubic Bézier curves that form it with dashed lines and the resulting path from offsetting the curves is the outer contour. (b) The 5×5 linear pattern to generate the lattice. (c) Isometric view of the final sample with its solid plates for testing.

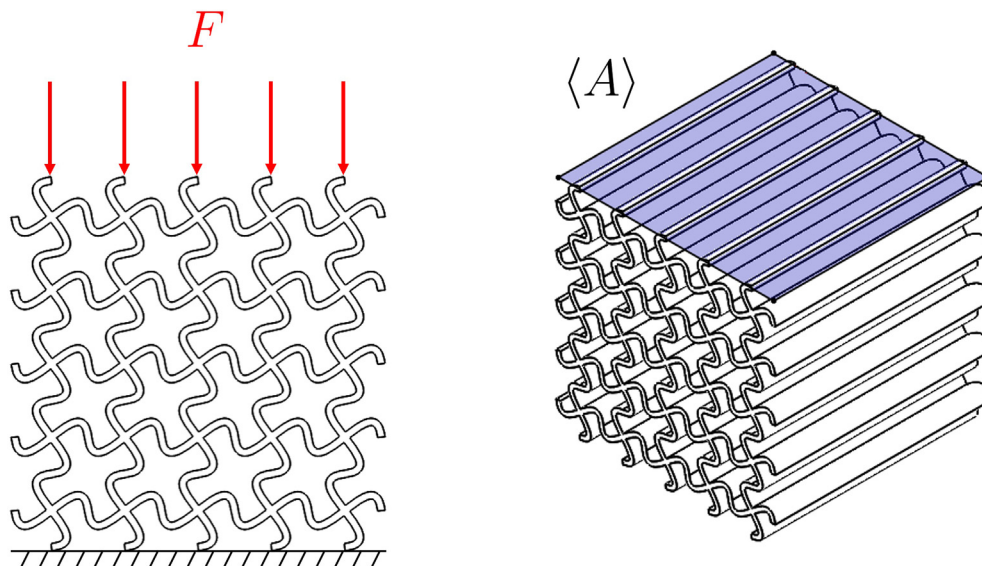


Fig. 7. Left: Boundary conditions for FEA simulation. Compressive load (top nodes) and fully fixed bottom nodes. Right: apparent area ($\langle A \rangle$) considered for calculating $\langle E \rangle$.

In the FEA models, a vertical compressive force of 0.2 N is applied in each of the five upper nodes for a total load $F = 1$ N. The five lower nodes are fully fixed. These boundary and loading conditions are depicted in Fig. 7. Since the maximum displacement corresponds to the upper nodes where the load is applied, the vertical displacement δ was measured at each node and averaged, resulting in the total displacement of the lattice sample.

3.3. Apparent mechanical properties calculation

The apparent Young's modulus is calculated as follows. Assuming a constant load distribution, the apparent stress $\langle \sigma \rangle$ is calculated by definition: $\langle \sigma \rangle = F/\langle A \rangle$, where $\langle A \rangle$ is the apparent area and it corresponds to the equivalent area of the whole lattice structure, which is normal to the applied load (i.e., the upper solid plate), see Fig. 7. The strain was obtained from the vertical displacement and the original length L of the lattice sample: $\varepsilon = \delta/L$. Hence, the apparent Young's modulus is obtained from the well-known stress-strain relation as: $\langle E \rangle = \langle \sigma \rangle/\varepsilon$.

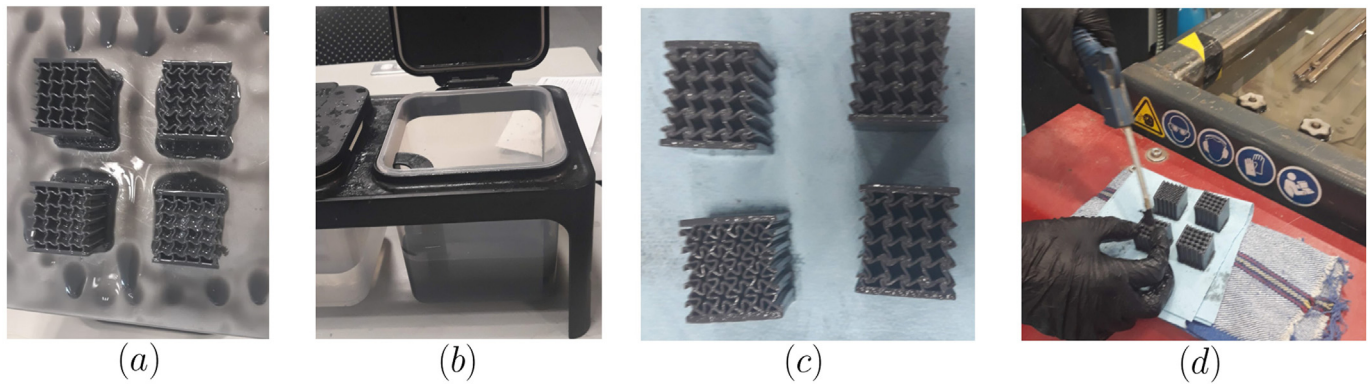


Fig. 8. (a) SBCB lattice samples in the building plate after printing is finished. (b) Washing with isopropyl alcohol. (c) Samples drying after washing with alcohol. (d) Samples being dried with compressed air.

The Young's modulus of the parent material was obtained by testing five dogbone tensile samples (according to ASTM D638, Type V), manufactured with the same printer, material, and printing orientation as the lattice samples. After this procedure, the average value obtained was 5.09 ± 0.07 MPa, value that was fed to the FEA model. All results will be presented based on the normalized apparent Young's modulus $\langle E \rangle / E$, where E is the Young's modulus of the parent material, to eliminate dependence on the base material and focus on the metamaterial topology.

3.4. Additive manufacturing of SBCB lattice samples

The samples were fabricated using the Form 2 SLA printer by Formlabs (Sommerville, United States). This family of printers builds up the part upside down, lifting the build platform at every layer to refill the resin tank. The resin used was *Flexible Resin* (version 2), produced by Formlabs, especially for its SLA printers. This resin is a mixture of methacrylic acid esters, photoinitiators, proprietary pigment, and additive package [35].

The set of previously generated 3D CAD files was converted to a set of STL files. These files are sliced by the Preform® software (Formlabs, Sommerville, United States) to generate the laser trajectories to cure the printing part. The models were arranged in batches of 4 samples each, centered at the building plate. Supports were generated

considering a support density of 0.7, a height of 1 mm over the base, and a contact point diameter of 0.8 mm. The resolution, or layer thickness, was set to $100 \mu\text{m}$.

The as-printed samples were washed in a vat filled with isopropyl alcohol to remove the excess of liquid resin. After taking the samples away from the alcohol, these were dried using compressed air. This step is needed to take away the excess resin and avoid its solidification during post-curing. Photographs of the main manufacturing stages are included in Fig. 8. Subsequently, they were post-cured with the aid of the *Form Cure* machine (Formlabs, Sommerville, United States), for 15 min at 60°C [36]. This to ensure stability in the mechanical properties of the SLA-samples even if they are further exposed to light, as reported in [37].

3.5. Additively manufactured lattice samples under compressive loadings

The effective mechanical properties of the SBCB structures were characterized under compressive loading, using a TVT6700 texture analyser (PerkinElmer, Waltham, United States). Three samples of each of the 20 designs were fabricated. The testing machine was set to a maximum vertical displacement of 15 mm for all tests. The top frame was set to move at a velocity of 1 mm/s. From the software TexCalc® the data corresponding to force F and displacement δ were exported to MATLAB® for further processing, obtaining the apparent

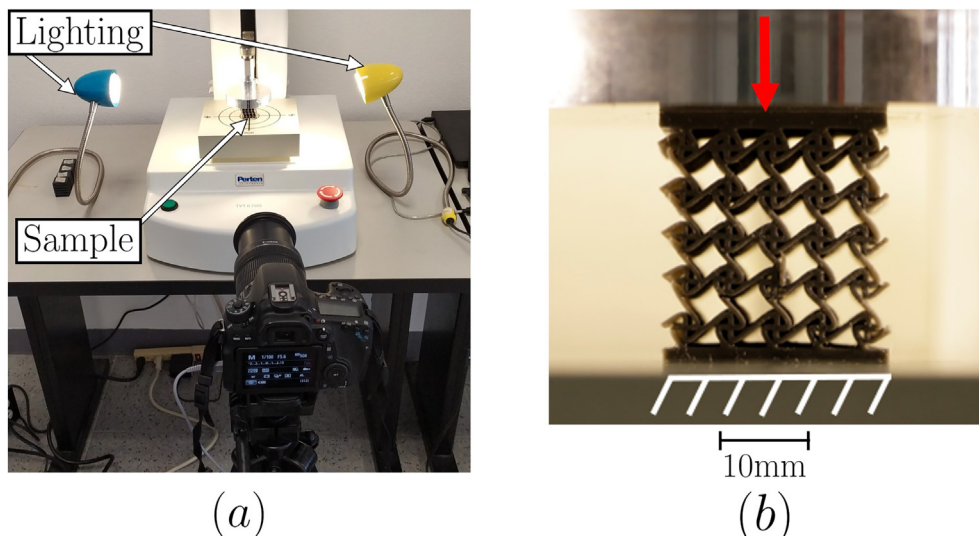


Fig. 9. (a) Mechanical characterization set up with camera and lighting. (b) Photo taken during the mechanical test, showing a lattice sample, indicating load direction and fixed support.

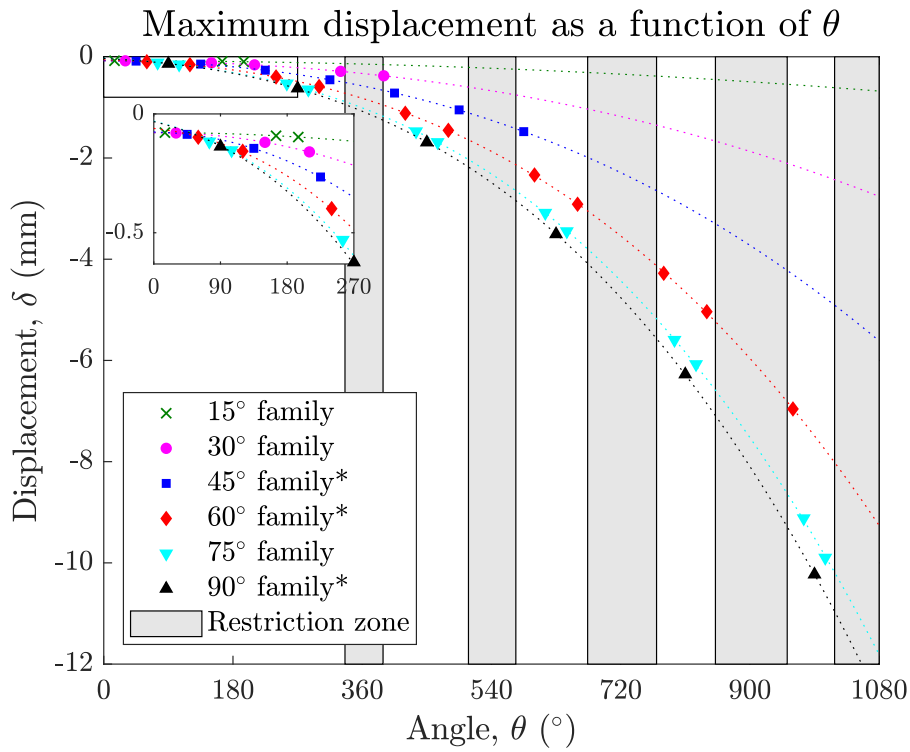


Fig. 10. Displacement δ obtained from FEA simulation of the compressive loadings, with respect to the angle θ defining the unit cell. Results are negative due to the direction of the force. Samples from families marked with an asterisk (45°, 60°, and 90°) were fabricated and are studied in the following sections.

Young's modulus $\langle E \rangle$ by converting the load-displacement plot to a strain-stress curve and obtaining the slope of the linear region. The

strain range for the linear region was set to be from zero to 3% because all models are linear in this range.

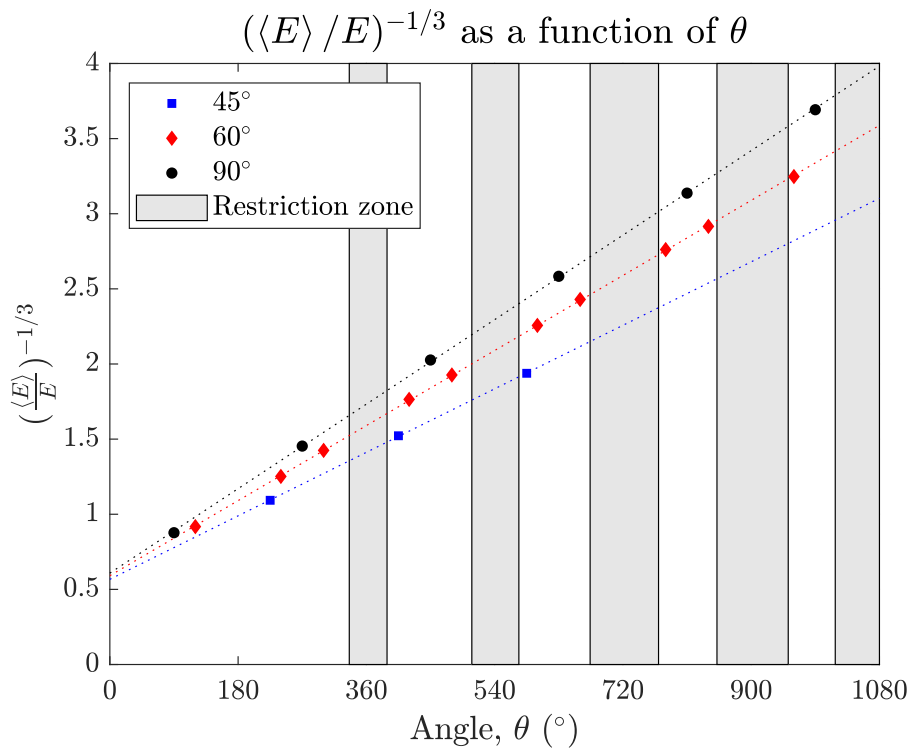


Fig. 11. Relation between $(\langle E \rangle / E)^{-1/3}$ and θ , for the 45°, 60°, and 90° SBCB lattice structure families.

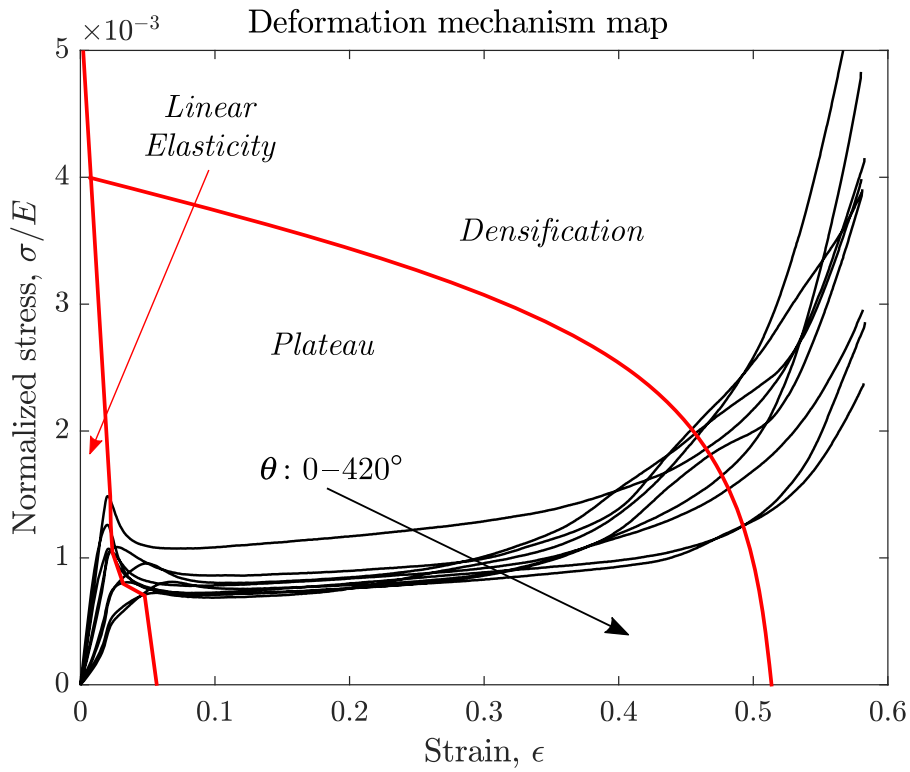


Fig. 14. Deformation mechanism map for the first nine SBCB structures, which show a plateau shape.

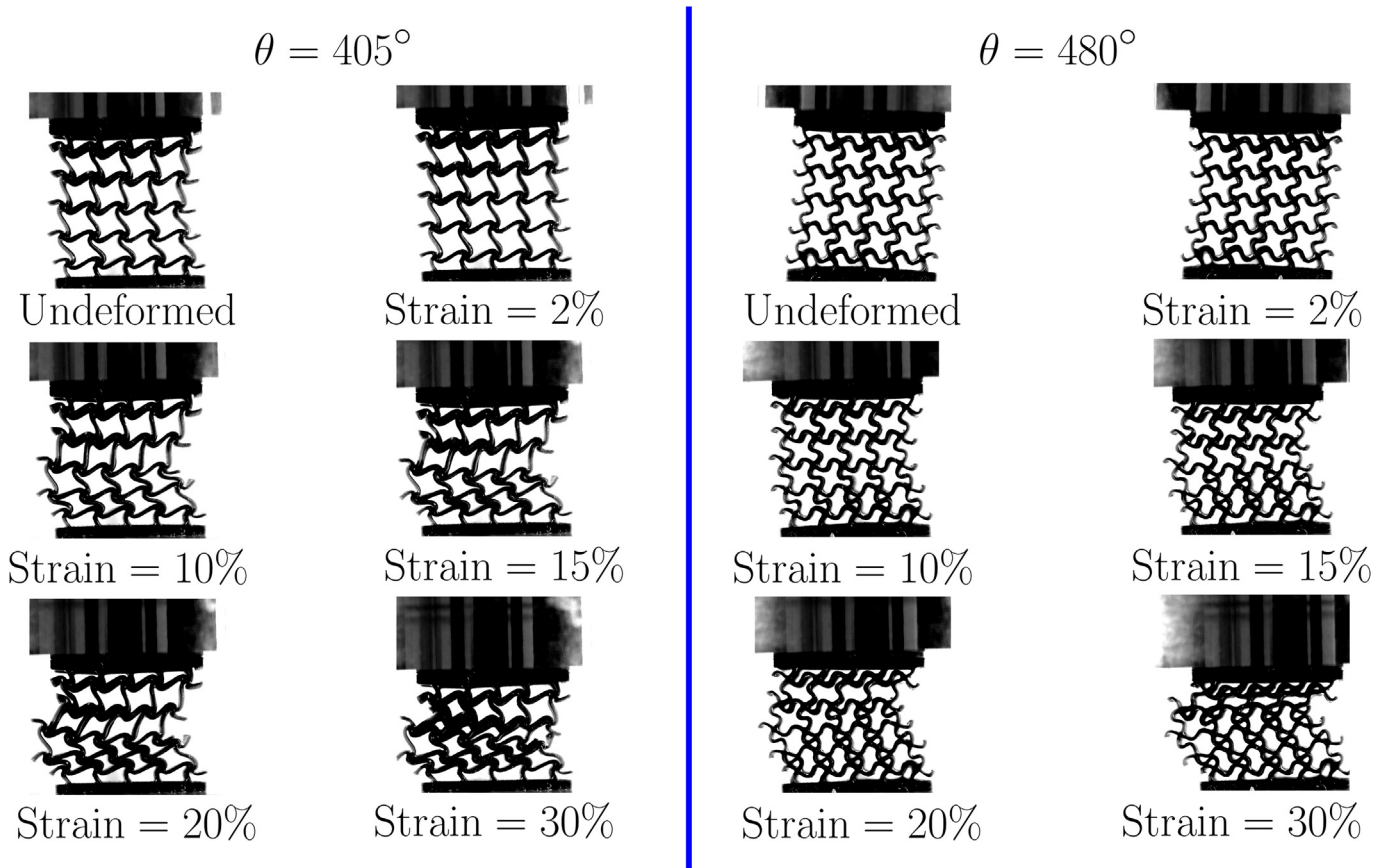


Fig. 15. Evolution of the deformed shape along the compression test. Left: a SBCB lattice structure presenting buckling. Right: a SBCB lattice structure entering densification immediately.

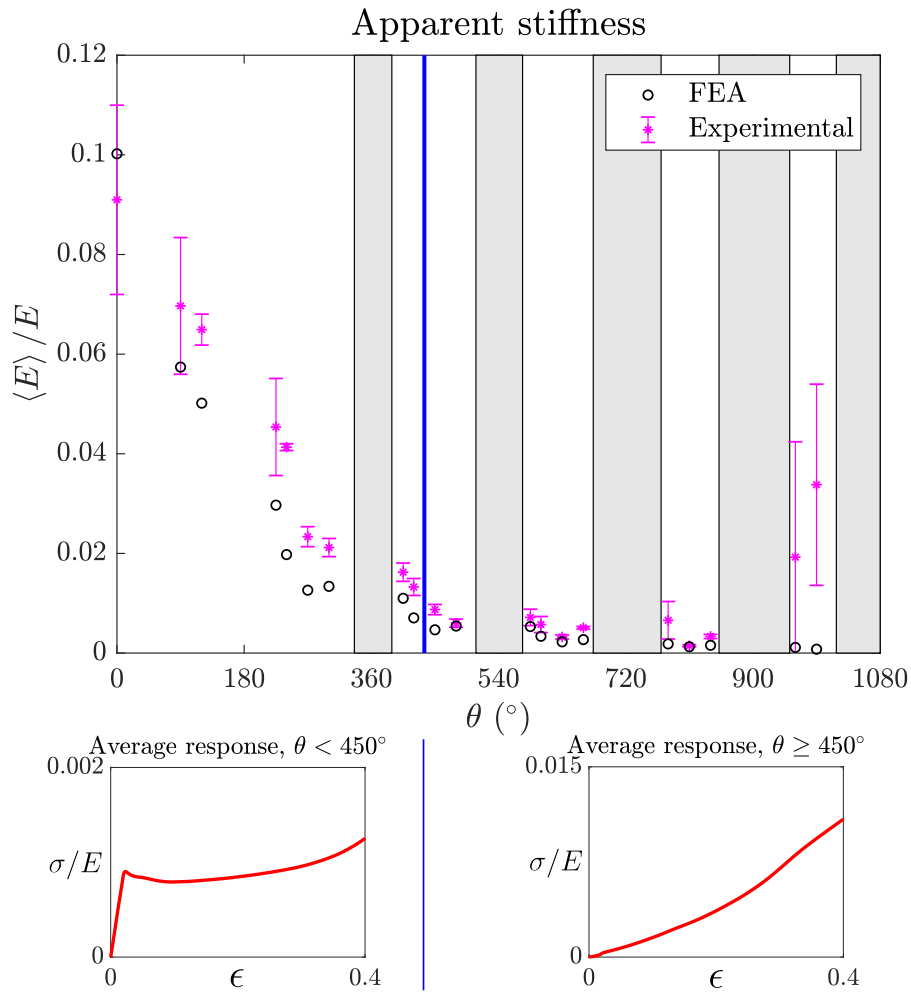


Fig. 16. Apparent stiffness: measurements and computations. Insets qualitatively show the average form of the stress-strain curve.

In order to track the deformation mechanism of every sample, a digital camera EOS70D (Canon, Tokyo, Japan) was set to shoot photos during the mechanical test regularly. The camera was set in continuous

mode, with an ISO of 500, lens aperture $f/5.6$, shutter speed $1/100$, and manual focus. Additional lighting was required as shown in Fig. 9a, and an example of the images taken is shown in Fig. 9b.

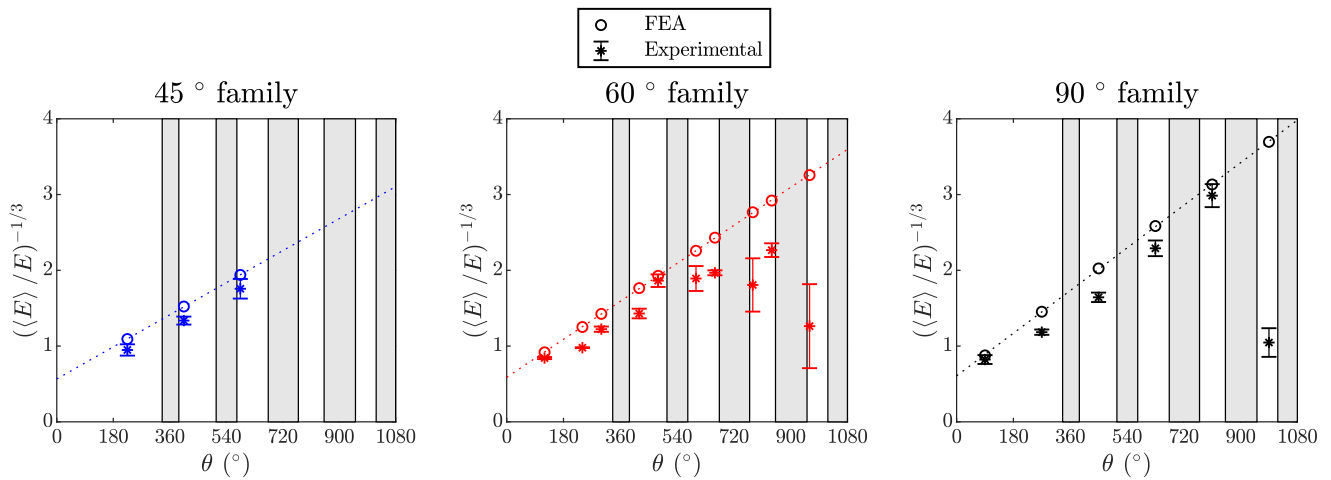


Fig. 17. Comparison between FEA and experimental data for the normalized Young's modulus $(E)/E$: total behaviour and behaviour within families of SBCB lattice structures.

4. Results

4.1. Apparent compressive stiffness characterized via FEA

Apparent stiffness was calculated from the vertical displacement, which is presented in Fig. 10 as a function of θ . Note that there are *restriction zones* in Fig. 10, which represent the SBCB structures that were not possible to be manufactured according to the curvature-thickness analysis (see Appendix).

The apparent Young's modulus $\langle E \rangle / E$ is calculated for each sample as defined on Section 3.3. The resulting values can be grouped by the previously defined families: 45°, 60°, and 90°. From the simulation results, the following mathematical relation was observed:

$$\frac{\langle E \rangle}{E} \propto \theta^{-3},$$

which holds for each family of SBCB lattice structures. When plotting $(\langle E \rangle / E)^{-1/3}$ versus θ , the points follow straight lines corresponding to a particular family. This is presented in Fig. 11.

An additional set of FEA simulations was performed varying the thickness t , and thus, the relative density. Results regarding the change in apparent stiffness due to changes in relative density are presented in Fig. 12. This computational model is a starting point for predicting the deformation mechanism of the samples. A stretch-dominated behaviour is observed for $\theta = 0$ with a linear apparent property-relative density relationship. While a bending-dominated behaviour is observed for $\theta = 120^\circ$, $\theta = 480^\circ$ and $\theta = 600^\circ$ with a non-linear apparent property-relative density relationship. This behaviour is observed with the increasing curvature in the relative density-stiffness plot.

4.2. Apparent compressive response: Measurements

Representative stress-strain curves measured from the compressive tests on the SBCB samples are presented in Fig. 13. The plots include snapshots of the sample during relevant instants of the mechanical test. A straight line starting from the origin is also included, which has a slope equal to the apparent Young's modulus $\langle E \rangle$ obtained from FEA simulations. The apparent stiffness of the SBCB structures shown are adequately predicted by the FEA model in their linear part. Recordings of the compressive-deformation stages of the four SBCB structures from the representative curves in Fig. 13 can be found in supplementary file V2.

Note from Fig. 13 that there are two representative forms of the stress-strain curves obtained. Compare representative curves (a) and (b) with (c) and (d). Fig. 13a–b show a linear region, a plateau due to elastic buckling, and a densification zone. These were qualitatively identified and placed in a *deformation mechanism map* for a range of SBCB structures, in accordance to Ashby [38] (Fig. 14). On the other hand, Fig. 13c–d show a permanent increase in stiffness. This behaviour is due to the almost immediate contact between curved lattice elements, leading to densification at the early stages of the compression tests. These can also be seen from inspecting Fig. 15, where photographs at different levels of strain are presented.

The SBCB lattice structure on the left in Fig. 15 presents buckling at their lattice element level. Since this structure has a low curvature, hence when compressed, their lattice elements are more prompt to buckling deformation, reflected in a plateau zone in their stress-strain curve. Moreover, the SBCB lattice structure on the right in Fig. 15 is conformed with lattice elements with higher curvature; upon compression, these elements get in contact with each other, leading to densification, hence presenting stiffness increment in the stress-strain curves.

A comparison of the apparent stiffness from both the experimental measurements and the computations calculation is included in Fig. 16.

After observing the representative strain-stress curve for each value of θ , it was concluded (qualitatively) that SBCB structures with $\theta < 450^\circ$ present the plateau region. The two forms of stress-strain curves are divided by a vertical line in Fig. 16, separating them into two main zones. The one on the left is conformed by the SBCB structures that present the plateau region, while the ones on the right present densification at earlier stages. Fig. 17 summarizes the experimental results for $\langle E \rangle$, and includes the experimental error separated by families. In the case of the family plots, they are also transformed to $(\langle E \rangle / E)^{-1/3}$, with ± 1 standard deviation error bars, and compared to the previously obtained FEA values from Fig. 11.

5. Discussion

The presented method for Bézier metamaterial synthesis offers a versatile approach for generating novel topologies. As all these new structures are mathematically parametrized, the understanding of their apparent mechanical properties could be explored systematically. Here we present a way of exploring different locations of the base control point P_1 by varying only the parameter θ . The method presented here can be expanded by adding more control points in a curved segment, provided that the slope continuity is kept. This means that the control points must have additional restrictions to ensure that the complete patterns are possible. The number, position, or orientation of curved segments per unit cell could also be modified. These possibilities show that the method presented here expands the possibilities of generating new families of metamaterials is far beyond the ones studied in this manuscript.

According to the FEA model, a dependence is observed between the angle θ and the apparent Young's modulus $\langle E \rangle$. Knowing that the distance r from P_1 to the origin is a multiple of θ , $\langle E \rangle$ decreases when moving the control point P_1 further away from the origin. This relationship $\langle E \rangle / E \propto r^{-3}$ is valid for all the models within the presented families of Bézier metamaterials. A longer distance from the origin to the location of P_1 produces a higher curvature, which in turn demands more material, resulting in higher relative densities. This fact for other topologies, results in a stiffer lattice metamaterial. However, here we demonstrate that higher curvature softens the structural response, even when the relative density has increased.

According to curved beam theories based on strain energy [39], upon the application of a tensile load, the deflection is proportional to the square of the radius of a curved element [40]. This radius is equivalent

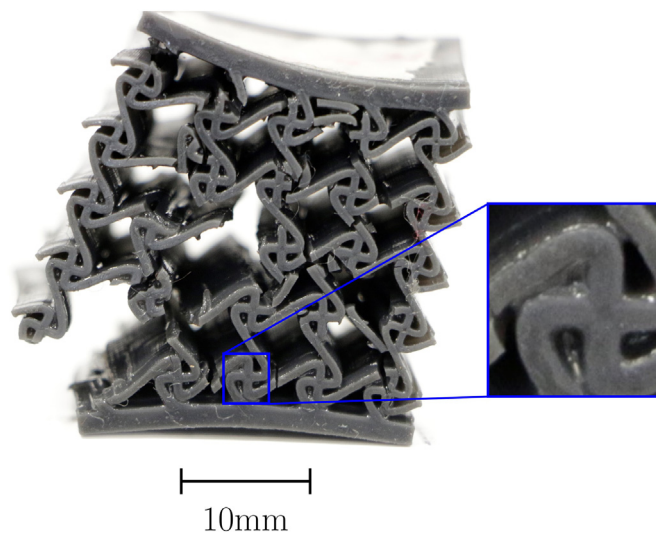


Fig. 18. Failure mode of a sample corresponding to $\theta = 780^\circ$. Curved elements stick to each other due to high curvature, undesired resin cured close to the intersections; hence increasing the overall stiffness.

to the distance r between point P_1 and the origin for the methodology presented here. The further away it is, the deflections will be smaller, and the structure will be stiffer. This result compares to the one found by Lei et al. [8] where elements with higher curvatures (comparable to higher values for r) are softer.

The deviations from FEA data obtained are higher when increasing θ . This can be explained with the increase in curvature. During the SLA postprocessing explained on Fig. 8, zones with a smaller radius of curvature are more prone to keep more liquid resin inside them, even after removing the excess resin with compressed air. This especially compromises material removal at the intersection between curved elements. When this liquid resin is cured, it becomes a solid defect (see Fig. 18) that increases the overall stiffness. Accumulation of non-desired material at the intersection of curved segments is more frequently encountered in SBCB structure samples with higher curvature.

6. Conclusions

In this work, we presented a versatile method for the synthesis of lattice metamaterials. The method used a cubic Bézier curve to conform the unit cell, which in turn conforms the lattice metamaterials. Here the structure is completely defined in terms of unit cell length λ and a parameter θ , which controls the location of the control point P_1 that defines the curve. In this work, computational models were created and used for both fabrication and simulations. The synthesis method can be further extended to include more control points or restrictions to the nature of a Bézier curve. While the present method was restricted to cubic Bézier curves, where only one control point was allowed to be placed at different locations to produce different lattice geometries, its applicability is far more powerful when using higher order curves.

A dependence was found between distance r from the origin and apparent Young's modulus $\langle E \rangle / E$, at a given direction θ . Deviations between FEA and experimental results can be explained in terms of

increasing curvature and its manufacturability challenges. The apparent stiffness of the Bézier-based metamaterials was successfully predicted using FEA simulations. Deviations from the computational predictions were attributed to manufacturing defects inherent to the samples fabricated. The lattice metamaterials generated in this work presented two main forms of stress-strain curves. The overall form of the stress-strain curve can be controlled with the degree of curvature of the Bézier curves used to conform the lattices. The synthesis of metamaterials with controlled stiffness can lead to the study of other mechanical properties such as Poisson's ratio and apparent shear modulus, enabling the structures to perform in various applications. Current work is being carried out on the variation of Poisson's ratio. Other applications where tailoring effective properties could be benefited from the synthesis method presented here. For instance, impact and shock absorbers, heat sink, porous structures for biomedical applications, among others.

Supplementary data to this article can be found online at <https://doi.org/10.1016/j.matdes.2020.109412>.

Data availability statement

The raw/processed data required to reproduce these findings cannot be shared at this time as the data also forms part of an ongoing study.

Declaration of Competing Interest

None.

Acknowledgements

This research was supported by Mexico's CONACYT Scholarship Program (Grant No. 1006922) and Project CB2016-285088. We also acknowledge Dr. Marcos Moya, MSc Víctor Romero, and Arturo Hernández, for their aid in the characterization and manufacturing

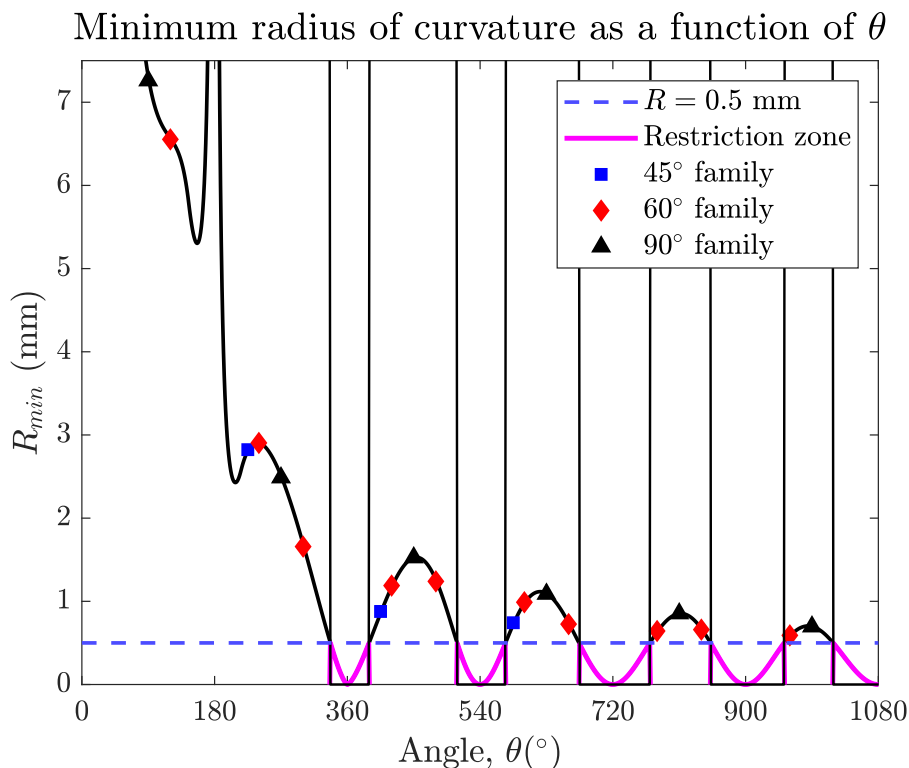


Fig. 19. Summary of all the minimum radii of curvature, for $\lambda = 10$. Markers indicate the studied designs, separated by families. The restriction zone is the set of all angles θ that make $R_{min} < 0.5$ mm.

techniques and facilities (CIMA) and Alicia Piña for guidance in digital photography and lighting. All this work has been done in the Metamaterials Lab at Tec de Mty, Querétaro.

Appendix: Curvature-thickness analysis

Here a mathematical derivation is presented for the *radius of curvature* (R) which must be no less than half the thickness of the Bézier curved elements of the unit cell. Expanding the Bézier curve parametric equation for $n = 3$ (Eq. (1)) and considering the conditions previously presented:

$$B(t) = P_0(1-t)^3 + 3P_1t(1-t)^2 + 3P_2t^2(1-t) + P_3t^3, \quad t \in [0, 1]$$

$$P_0 = (-\lambda/2, 0); \quad P_1 = (x_1, y_1); \quad P_2 = (-x_1, -y_1); \quad P_3 = (\lambda/2, 0)$$

Given that the control points P_n are complex numbers, separating Eq. (1) into its real and imaginary parts yields two separate equations representing the x - and y - coordinates of the points conforming the curve:

$$x(t) = 3x_1t - 9x_1t^2 + 6x_1t^3 - \lambda/2 + 3\lambda t/2 - 3\lambda t^2/2 + \lambda t^3$$

$$y(t) = 3y_1t - 9y_1t^2 + 6y_1t^3,$$

being $x(t)$ and $y(t)$ the x - and y - coordinates of a point in the curve given the parameter t , which goes from 0 to 1.

The initial coordinates (x_1, y_1) are a function of the initial parameter θ . This function is defined from the equation of the governing spiral in polar coordinates: $r(\theta) = \lambda\theta/4\pi$. Then, for a given angle θ , the coordinates of the control point P_1 can be obtained by changing the previous definition to Cartesian coordinates:

$$(x_1, y_1) = (r \cos \theta, r \sin \theta) = \left(\frac{\lambda\theta \cos \theta}{4\pi}, \frac{\lambda\theta \sin \theta}{4\pi} \right)$$

The radius of curvature R for this particular curve [41], in terms of θ as the parameter t changes, is defined as:

$$R(\theta, t) = \frac{3\lambda(\pi^2\theta^2u^2 + 4\pi\theta uv \cos \theta + 4v^2)^{3/2}}{32\pi(2t-1)\theta \sin \theta}, \quad (3)$$

with $u = 6t^2 - 6t + 1$ and $v = 2t^2 - 2t + 1$, $t \in [0, 1]$. Eq. (3) is minimized with respect to t , inside the interval $[0, 1]$. The minimum values corresponding to all values of θ , for $\lambda = 10$, are plotted in Fig. 19. All designs with $R_{min} < 0.5$ mm are not manufacturable with the previous definitions for unit cell synthesis.

References

- [1] J.B. Berger, H.N. Wadley, R.M. McMeeking, Mechanical metamaterials at the theoretical limit of isotropic elastic stiffness, *Nature* 543 (7646) (2017) 533–537, <https://doi.org/10.1038/nature21075>.
- [2] A. Nazir, K.M. Abate, A. Kumar, J.-Y. Jeng, A state-of-the-art review on types, design, optimization, and additive manufacturing of cellular structures, *Int. J. Adv. Manuf. Technol.* (2019) <https://doi.org/10.1007/s00170-019-04085-3>.
- [3] K. Refai, M. Montemurro, C. Brugger, N. Saintier, Determination of the effective elastic properties of titanium lattice structures, *Mech. Adv. Mater. Struct.* 0 (0) (2019) 1–14, <https://doi.org/10.1080/15376494.2018.1536816>.
- [4] T.A. Schaedler, A.J. Jacobsen, A. Torrents, A.E. Sorensen, J. Lian, J.R. Greer, L. Valdevit, W.B. Carter, Ultralight metallic microlattices, *Science* 334 (6058) (2011) 962–965, <https://doi.org/10.1126/science.1211649>.
- [5] X. Wang, S. Xu, S. Zhou, W. Xu, M. Leary, P. Choong, M. Qian, M. Brandt, Y.M. Xie, Topological design and additive manufacturing of porous metals for bone scaffolds and orthopaedic implants: a review, *Biomaterials* 83 (2016) 127–141, <https://doi.org/10.1016/j.biomaterials.2016.01.012>.
- [6] S.J. Hollister, Porous scaffold design for tissue engineering, *Nat. Mater.* 4 (7) (2005) 518–524, <https://doi.org/10.1038/nmat1421>.
- [7] G. Savio, S. Rosso, R. Meneghello, G. Concheri, Geometric modeling of cellular materials for additive manufacturing in biomedical field: a review, *Appl. Bionics Biomech.* 2018 (2018) <https://doi.org/10.1155/2018/1654782>.
- [8] M. Lei, W. Hong, Z. Zhao, C. Hamel, M. Chen, H. Lu, H.J. Qi, 3D printing of auxetic metamaterials with digitally reprogrammable shape, *ACS Appl. Mater. Interf.* (October) (2019) <https://doi.org/10.1021/acsami.9b06081>.
- [9] M. Kuczewicz, P. Baranowski, J. Małachowski, A. Popławski, P. Piatek, Modelling, and characterization of 3D printed cellular structures, *Mater. Des.* 142 (February) (2018) 177–189, <https://doi.org/10.1016/j.matdes.2018.01.028>.
- [10] M. Kuczewicz, P. Baranowski, M. Stankiewicz, M. Konarzewski, P. Piatek, J. Małachowski, Modelling and testing of 3D printed cellular structures under quasi-static and dynamic conditions, *Thin-Walled Struct.* 145 (August) (2019) 106385, <https://doi.org/10.1016/j.tws.2019.106385>.
- [11] X. Yang, Y. Sun, J. Yang, Q. Pan, Out-of-plane crashworthiness analysis of bio-inspired aluminum honeycomb patterned with horseshoe mesostructure, *Thin-Walled Struct.* 2018 (September 2017) 1–11, <https://doi.org/10.1016/j.tws.2018.01.014>.
- [12] J.C. McCaw, E. Cuan-Urquiza, Curved-layered additive manufacturing of non-planar, parametric lattice structures, *Mater. Des.* 160 (2018) 949–963, <https://doi.org/10.1016/j.matdes.2018.10.024>.
- [13] J.C. McCaw, E. Cuan-Urquiza, Mechanical characterization of 3d printed, non-planar lattice structures under quasi-static cyclic loading, *Rapid Prototyp. J.* 64 (4) (2020) 707–717, <https://doi.org/10.1108/RPJ-06-2019-0163>.
- [14] Z.P. Wang, L.H. Poh, Optimal form and size characterization of planar isotropic petal-shaped auxetics with tunable effective properties using IGA, *Compos. Struct.* 201 (June) (2018) 486–502, <https://doi.org/10.1016/j.compstruct.2018.06.042>.
- [15] Z.P. Wang, L.H. Poh, Y. Zhu, J. Dirrenberger, S. Forest, Systematic design of tetrapetals auxetic structures with stiffness constraint, *Mater. Des.* 170 (June) (2019) <https://doi.org/10.1016/j.matdes.2019.107669>.
- [16] J. Dirrenberger, S. Forest, D. Jeulin, Effective elastic properties of auxetic microstructures: anisotropy and structural applications, *Int. J. Mech. Mater. Des.* 9 (1) (2013) 21–33, <https://doi.org/10.1007/s10999-012-9192-8>.
- [17] A. Alomarah, D. Ruan, S. Masood, I. Sbarski, B. Faisal, An investigation of in-plane tensile properties of re-entrant chiral auxetic structure, *Int. J. Adv. Manuf. Technol.* 96 (5–8) (2018) 2013–2029, <https://doi.org/10.1007/s00170-018-1605-x>.
- [18] H. Ebrahimi, D. Mousanezhad, H. Nayeib-Hashemi, J. Norato, A. Vaziri, 3D cellular metamaterials with planar anti-chiral topology, *Mater. Des.* 145 (2018) 226–231, <https://doi.org/10.1016/j.matdes.2018.02.052>.
- [19] Y. Zhu, Z. Zeng, Z.-P. Wang, L.H. Poh, Y. Shao, Hierarchical hexachiral auxetics for large elasto-plastic deformation, *ACS Appl. Mater. Interfaces* 6 (8) (2019) <https://doi.org/10.1088/2053-1591/ab1a22>.
- [20] M.J. Choi, S. Cho, Isogeometric configuration design optimization of shape memory polymer curved beam structures for extremal negative Poisson's ratio, *Struct. Multidiscip. Optim.* 58 (5) (2018) 1861–1883, <https://doi.org/10.1007/s00158-018-2088-y>.
- [21] H.N. Fitter, A.B. Pandey, D.D. Patel, J.M. Mistry, A review on approaches for handling Bézier curves in CAD for manufacturing, *Proced. Eng.* 97 (2014) 1155–1166, <https://doi.org/10.1016/j.proeng.2014.12.394>.
- [22] X. Xiao, M. Sabin, F. Cirak, Interrogation of spline surfaces with application to isogeometric design and analysis of lattice-skin structures, *Comput. Methods Appl. Mech. Eng.* 351 (2019) 928–950, <https://doi.org/10.1016/j.cma.2019.03.046>.
- [23] H. Deng, S. Hinnebusch, A. C. To, Topology optimization design of stretchable metamaterials with Bézier skeleton explicit density (BSED) representation algorithm, *Comput. Methods Appl. Mech. Eng.* 366 (2020) 1–30, <https://doi.org/10.1016/j.cma.2020.113093>.
- [24] D. Bourell, J.P. Kruth, M. Leu, G. Levy, D. Rosen, A.M. Beese, A. Clare, Materials for additive manufacturing, *CIRP Ann. Manuf. Technol.* 66 (2) (2017) 659–681, <https://doi.org/10.1016/j.cirp.2017.05.009>.
- [25] I. Cotabarren, C.A. Palla, C.T. McCue, A.J. Hart, An assessment of the dimensional accuracy and geometry-resolution limit of desktop stereolithography using response surface methodology, *Rapid Prototyp. J.* 25 (7) (2019) 1169–1186, <https://doi.org/10.1108/RPJ-03-2019-0060>.
- [26] S. Park, A.M. Smallwood, C.Y. Ryu, Mechanical and thermal properties of 3d-printed thermosets by stereolithography, *J. Photopolym. Sci. Technol.* 32 (2) (2019) 227–232, <https://doi.org/10.2494/photopolymer.32.227>.
- [27] Y. Yang, L. Li, J. Zhao, Mechanical property modeling of photosensitive liquid resin in stereolithography additive manufacturing: bridging degree of cure with tensile strength and hardness, *Mater. Des.* 162 (2019) 418–428, <https://doi.org/10.1016/j.matdes.2018.12.009>.
- [28] M.P. Watters, M.L. Bernhardt, Curing parameters to improve the mechanical properties of stereolithographic printed specimens, *Rapid Prototyp. J.* 24 (1) (2018) 46–51, <https://doi.org/10.1108/RPJ-11-2016-0180>.
- [29] D. Lin, S. Jin, F. Zhang, C. Wang, Y. Wang, C. Zhou, G.J. Cheng, 3D stereolithography printing of graphene oxide reinforced complex architectures, *Nanotechnology* 26 (43) (2015) <https://doi.org/10.1088/0957-4484/26/43/434003>.
- [30] D.K. Patel, A.H. Sakhaei, M. Layani, B. Zhang, Q. Ge, S. Magdassi, Highly stretchable and UV curable elastomers for digital light processing based 3D printing, *Adv. Mater.* 29 (15) (2017) 1–7, <https://doi.org/10.1002/adma.201606000>.
- [31] M. Keshavarzan, M. Kadkhodaei, M. Badrossamay, M.R. Karamooz Ravari, Investigation on the failure mechanism of triply periodic minimal surface cellular structures fabricated by Vat photopolymerization additive manufacturing under compressive

- loadings, *Mech. Mater.* 140 (August 2019) (2020) 103150, <https://doi.org/10.1016/j.mechmat.2019.103150>.
- [32] L. Shi, W. Zhang, Y. Cheng, Z. Deng, Gravity aided inertial navigation path planning algorithm based on underwater vehicle constraint and bezier curve, *Proceedings of the 38th Chinese Control Conference 2019*, pp. 3857–3862, <https://doi.org/10.23919/ChiCC.2019.8866183>.
- [33] 4-Node Structural Shell, URL https://www.mm.bme.hu/~gyebro/files/ans_help_v182/ans_elem/Hlp_E_SHELL181.html Jul 2017.
- [34] Formlabs, Flexible Resin for Features, URL https://formlabs-media.formlabs.com/datasheets/Flexible_Technical.pdf 2017.
- [35] Formlabs, Photoreactive Resin for Form 1+ MATERIAL SAFETY DATA SHEET, 2014.
- [36] Formlabs, Post-Curing with Form Cure, 2020.
- [37] F. Jiang, D. Drummer, Curing kinetic analysis of acrylate photopolymer for additive manufacturing by photo-DSC, *Polymers* 12 (5) (2020) 1–11, <https://doi.org/10.3390/POLYM12051080>.
- [38] M.F. Ashby, Mechanical Properties of Cellular Solids, *Metal. Trans. A, Phys. Metal. Mater. Sci.* 14 A (9) (1983) 1755–1769, <https://doi.org/10.1007/BF02645546>.
- [39] Y. Gangamwar, V. Deo, S. Chate, M. Bhandare, P.H.N. Deshpande, Determination of curved beam deflection by using castigliano's theorem, *Int. J. Res. Emerg. Sci. Technol.* 3 (2016) 19–24.
- [40] R.G. Budynas, J.K. Nisbett, et al., *Shigley's Mechanical Engineering Design*, Vol. 10, McGraw-Hill New York, 2014.
- [41] P. Gupta, Curvature and torsion, *Topics in Differential Geometry* 2019, pp. 35–86.